A Scalable Fishbone Nanowire Array (FINE) for 3D Quasi-Intracellular Recording in Intact Brains

*Youngbin Tchoe, Jihwan Lee, Karen J. Tonsfeldt, Tianhai Wu, Daniel R. Cleary, Hoi Sang U, Ren Liu, Guy Bouvier, Ritwik Vatsyayan, Andrew M. Bourhis, Sang Heon Lee, Eric Halgren, Ian Galton, Massimo Scanziani, and Shadi A. Dayeh**

Intracellular recordings provide unique access to the submillisecond neuronal membrane potential changes, revealing dynamics that orchestrate cellular, local, and large-scale brain activity. However, technical requirements limit the scalability of intracellular recordings to large populations of neurons, especially within intact brains. To overcome this limitation, a Fishbone Intracellular Nanowire Electrode (FINE) is developed with ultra-sharp nanowire tips strategically integrated at slanted angles along an implantable shank to record 3D intracellular potentials from ensembles of neurons in intact brain. A novel fabrication process is developed to integrate reverse-angled platinum silicide (PtSi) nanowires to preserve the structural integrity of FINE during insertion. As-implanted or sub-micron retraced FINE spreads the PtSi nanowires away from the shank to establish intimate nanowire-neuron interfaces that yield quasi-intracellular potentials. Comparative analyses of nanowire recordings versus adjacent planar recordings on the same shank validate their distinctive quasi-intracellular recording characteristics. The scalability of FINE is demonstrated to a 3D 24-shank array with 594 nanowires and 430 planar contacts and successfully identified quasi-intracellular potentials across 127 distinct nanowires in the intact brain. FINE's 3D quasi-intracellular recording holds the potential to unlock detailed investigations of the intricate ionic potential fluctuations and patterns of transmembrane potentials that drive behavior and cognition.

1. Introduction

Intracellular electrophysiological recordings, most commonly performed with sharp microelectrodes or with patch clamp electrodes for whole cell recordings, offer unparalleled access to minute fluctuations of neuronal membrane potentials thereby revealing the subthreshold electrical activity of neurons.[1,2] Substantial innovations have expanded these techniques from single to multiple neurons and from the in vitro to the in vivo settings within intact brains including in behaving animals.[3] Automated systems now make whole cell recordings less cumbersome, thereby enhancing their utility in both in vitro and in vivo settings.[4,5] The nature of the whole cell recording technique, however, severely limits the number of neurons that can be recorded simultaneously in vivo, and those neurons are generally located in the more accessible (i.e., superficial) structures of the brain. Furthermore, whole cell recordings from intact brains generally need to be performed in head-fixed animals.[5,6] To overcome these limitations, there is a need for

Y. Tchoe, J. Lee, K. J. Tonsfeldt, T. Wu, D. R. Cleary, H. S. U, R. Liu,
R. Vatsyayan, A. M. Bourhis, S. H. Lee, S. A. Dayeh
Integrated Electronics and Biointerfaces Laboratory
Department of Electrical and Computer Engineering
University of California San Diego
La Jolla, CA 92093, USA
E-mail: sdayeh@ucsd.edu

Y. Tchoe
Department of Biomedical Engineering
Ulsan National Institute of Science and Technology
Ulsan 44919, South Korea

K. J. Tonsfeldt
Department of Obstetrics, Gynecology, and Reproductive Sciences
Center for Reproductive Science and Medicine
University of California San Diego
La Jolla, CA 92093, USA

D. R. Cleary, M. Scanziani
Department of Neurological Surgery
University of California San Diego
La Jolla, CA 92093, USA

G. Bouvier
Department of Physiology
University of California San Francisco
San Francisco, CA 94143, USA

E. Halgren
Department of Radiology
University of California San Diego
La Jolla, CA 92093, USA

I. Galton
Department of Electrical and Computer Engineering
University of California San Diego
La Jolla, CA 92093, USA

The ORCID identification number(s) for the author(s) of this article can be found under https://doi.org/10.1002/adma.202504171

DOI: 10.1002/adma.202504171

new, scalable technologies to record intracellular electrical activity from a large number of neurons in intact brains. Such technology will dramatically improve the scope of neuronal recording and deepen our understanding of the brain activities underlying behavior and cognition.

Nanoscale electrode arrays have emerged as promising candidates for establishing intracellular interfaces with multiple neurons.[7–14] These arrays, which are often integrated onto microelectrode array chips, record intracellular potentials through mechanisms that include electroporation[7] or natural internalization[8] in in vitro settings. Though nanoelectrode technologies have been deployed in vivo,[9,10] they have so far only recorded extracellular neuronal potentials. Simultaneously recording intracellular potentials of numerous neurons would offer the capability to precisely track and more precisely deconstruct fine neural circuits. To translate these advanced nanoscale electrodes for in vivo intracellular recordings, entirely new approaches in material synthesis and fabrication are necessary.

We developed the Fishbone Intracellular Nanowire Electrode (FINE) to deliver nanowire electrodes across the depth of an intact brain and to achieve simultaneous intracellular recordings from tens, hundreds, and potentially thousands of neurons. The nanowire electrodes have sub-100 nm sharp tips which are positioned at slanted, reverse angles from the carrier shank body in a fishbone-like pattern. The hard nanowires are engineered with a polycrystalline platinum silicide alloy which achieves azimuthal flexibility when embedded in thin polyimide and parylene films. This unique configuration provides flexibility upon insertion to the brain, preserving the structural integrity of the nanowires, and controlled expandability by submicron retraction to reach and to establish intimate interfaces with nearby neurons in intact brains. Once fully implanted, FINE recorded quasi-intracellular potentials from 127 different channels for the first time in an intact brain.

2. Results

2.1. Fabrication of Fishbone Intracellular Nanowire Electrode

FINE consists of nanowires, planar contacts, and metal traces constructed via a series of nanofabrication steps. These components are embedded within dual-layer flexible polymer sheets, consisting of polyimide (700 nm) and parylene C (700 nm) layers as shown in the exploded view schematics of FINE (**Figure 1a**). An SU-8, a negative-tone epoxy photoresist, polymer shank with a thickness of 50 µm and a length of 1.8 mm, implemented as a final microfabrication step, is included as a stiffener to provide rigidity for penetrating the rat cortex (Figure 1b).

The key actuation mechanism for recording quasi-intracellular potentials is illustrated in Figure 1c. When inserted, the reverse-angled nanowires bend toward the shank, and, after reaching the target depth, FINE can be retracted by less than a micron to expand the nanowires outward from the shank and toward neuronal cell bodies. The optical microscopy image (Figure 1d) shows representative well-defined 50 PtSi nanowires along each side of the shank together with 18 planar contacts, each of which has a diameter of 30 µm, positioned on the midline of the shank. Out of 50 nanowires, 25 are connected to metal leads, and all 18 planar contacts are interconnected with metal traces. The SU-8-based shank has a length of 1.8 mm and a width that tapers from 400 µm down to 8 µm near the tip. Scanning Electron Microscopy (SEM) images (Figure 1e) show the layered structure of FINE and the polymer-embedded nanowire tips. The Au planar contacts are exposed through a thin polyimide passivation layer of thickness of 700 nm. The PtSi nanowires were passivated by embedding them in polyimide and parylene C layers, each with a thickness of 700 nm. The details of the microfabrication process are provided in Figure S1 (Supporting Information) of the supplementary materials.

The planar PtSi nanowires were fabricated using e-beam lithography (E of an e-beam resist bilayer (PMMA 495K/EL6), followed by sequential deposition of Cr/Pt/Si/Pt/Si/Pt/Cr layers (5/80/80/160/80/80/5 nm) via directional sputtering, lift-off, and thermal annealing at 350 °C in N_2 atmosphere. Conventional co-sputtering was used to fill the undercut regions of the e-beam resist layers, resulting in undesired vertical films around the nanowire tips, and the directionally sputtered PtSi nanowires exhibited a clean, sharply pointed tip geometry (Figure S2, Supporting Information). Furthermore, our study on annealing much thicker, multilayer stacks of Pt and Si thin films (each with layer thickness up to 500 nm) demonstrated that thermal annealing effectively intermixed the Pt and Si, producing a PtSi alloy with a homogeneous composition (Figure S3, Supporting Information). The PtSi nanowires were developed through multiple batches of microfabrication processes as shown in the SEM images in Figure S4 (Supporting Information). The optimized PtSi nanowire tips exhibit desirable properties including sub-100 nm sharp tips, robustness, and effective insulation layers. The overall yield of nanowires with good passivation, defined by a 1 kHz impedance above 500 kΩ, was estimated to be 84% and 89% in two representative cases (Figure S5, Supporting Information).

We characterized the crystallinity, mechanical, and electrical properties of FINE's PtSi nanowires. X-ray diffraction (XRD) theta-2theta on a co-sputtered PtSi film demonstrated a transition from an amorphous PtSi (*a*-PtSi) as deposited film to a polycrystalline PtSi (*poly*-PtSi) structure after thermal annealing at 350 °C as shown in Figure 1f. Prior to annealing, the film exhibited broad diffraction peaks indicative of the amorphous Si and Pt composition. After annealing, the peaks were seen to have become well-defined, distinct peaks, characteristic of the Pt_2Si phase. We evaluated the mechanical properties of Pt, *a*-PtSi, and *poly*-PtSi to determine if alloying and poly-crystallization could improve nanowire hardness (Figure 1g). The hardness of *a*-PtSi was more than twice as high as that of Pt, and thermally annealing PtSi to form *poly*-PtSi led to an additional 30% increase in hardness. Meanwhile, the elastic moduli of both *a*-PtSi and *poly*-PtSi remained comparable to that of Pt. The increase in hardness of *poly*-PtSi, while maintaining a similar elastic modulus to Pt offers improved resistance to crystal deformation while preserving

---

S. A. Dayeh
Department of Bioengineering
Department of Nanoengineering
Department of Neurological Surgery
and Materials Science and Engineering Program
University of California San Diego
La Jolla, CA 92093, USA

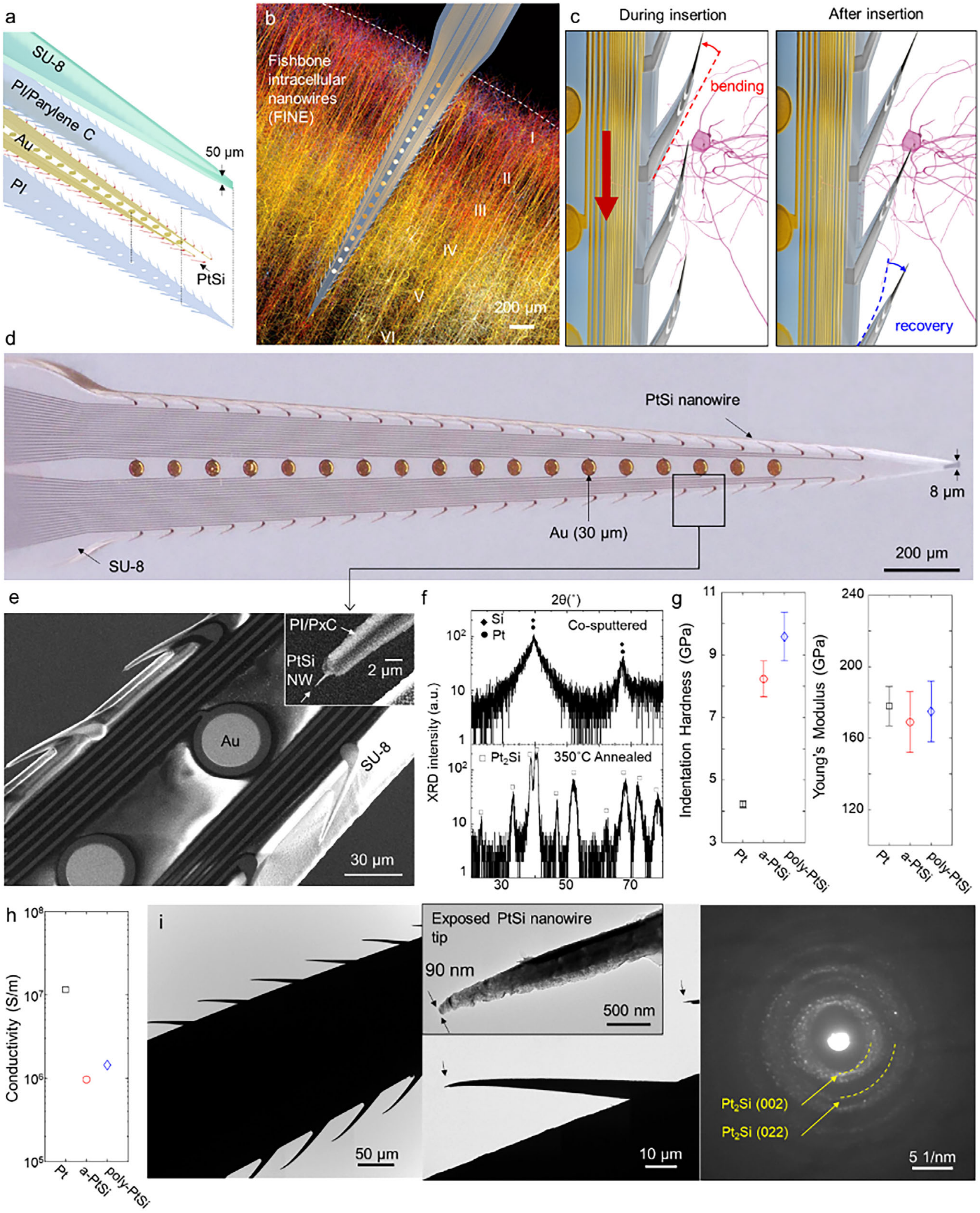
a
SU-8
PI/Parylene C
Au
PI
50 μm
PtSi
b
Fishbone intracellular nanowires (FINE)
I
II
III
IV
V
VI
200 μm
c
During insertion
After insertion
bending
recovery
d
PtSi nanowire
8 μm
Au (30 μm)
SU-8
200 μm
e
PI/PxC
PtSi NW
2 μm
Au
SU-8
30 μm
f
2θ(°)
Si
Pt
Co-sputtered
XRD intensity (a.u.)
Pt₂Si
350°C Annealed
10²
10
1
30
50
70
g
Indentation Hardness (GPa)
11
9
7
5
3
Pt
a-PtSi
poly-PtSi
Young's Modulus (GPa)
240
200
160
120
h
Conductivity (S/m)
10⁸
10⁷
10⁶
10⁵
i
Exposed PtSi nanowire tip
90 nm
500 nm
50 μm
10 μm
Pt₂Si (002)
Pt₂Si (022)
5 1/nm

flexibility and torque resilience. The six-point probe conductivities of Pt, *a*-PtSi, and *poly*-PtSi films were 1.2×10^7, 9.6×10^5, and 1.4×10^6 S m^{-1}, respectively (Figure 1h). The conductivity of *a*-PtSi decreased to 13 times less than that of Pt; however, *poly*-PtSi, formed by subsequent thermal annealing, showed a 50% increase in conductivity compared to *a*-PtSi. Although the conductivity of the *poly*-PtSi alloy is 9 times lower than that of Pt, it is on par with other metal conductivities including stainless steel (1.45×10^6 S m^{-1})[11] and far higher than semiconductor nanowires including highly-doped, crystalline Si (10^3 S m^{-1}).[12,13] The 1 kHz electrochemical impedance of the *poly*-PtSi nanowires is 6 ± 4 MΩ (Figure S5, Supporting Information). Our earlier work have shown that the electrochemical impedance of nanowires, regardless of their material composition such as AgCl/Ag, Pt, or Si, exhibits predominantly capacitive behavior, likely due to geometric effects having a greater influence than the surface electrochemical effects.[14] We expect PtSi nanowires to display a similar capacitive behavior. Bright-field transmission electron microscopy (TEM) in Figure 1i and high-resolution TEM (HR-TEM) revealed a distribution of *poly*-PtSi with sharp tips with tip diameters of 90 nm positioned on each side of the shank. The concentric diffraction rings from a *poly*-PtSi nanowire confirmed the successful formation of polycrystalline Pt_2Si microstructure at the single nanowire level. Notably, the 90 nm sharp nanowire tips of FINE are smaller than the 200 nm tip diameters of vertical nanowire arrays which demonstrated the capability of penetration of neuronal membranes and recording of intracellular potentials from neurons in vitro.[15]

2.2. Quasi-Intracellular Recording from the Intact Brain with FINE

To assess the electrophysiological recording capabilities of FINE, we implanted several FINEs in a head-fixed rat brain and performed recordings under ketamine/xylazine anesthesia. A single-shank FINE, composed of 25 nanowires and 18 planar contacts, was slowly inserted into the brain at a speed ranging from 2 to 10 μm s^{-1} using a motorized linear actuator with a stereotactic adaptor (Neuronexus Technologies, Inc.) to a target depth of 2 mm. The shank, primarily made of 50-μm-thick SU-8, featured a sharply pointed tip that exhibited sufficient stiffness for cortical penetration. The electrical potential at the tip of each nanowire was measured relative to a reference needle inserted into the scalp muscle near the neck. Electrophysiological recording was initiated prior to the insertion of FINE and continued until its removal from the brain. Upon completing the insertion of the FINE to its target depth, intracellular-like activities were sometimes absent or limited to only a few channels possibly by acute trauma from cells. Improved recordings were consistently produced upon fine mechanical tuning of FINE in submicron-scale steps. The real-time monitoring provided feedback used to advance or retract FINE by 0.4 μm steps until we detected high-amplitude spikes from several nanowire channels.

The nanowire channels of FINE recorded a few millivolt-level amplitude spikes from the intact brain, as depicted in the representative waveform in **Figure 2a**. These spikes, recorded by the nanowire channels featuring both millivolt-level amplitude and positive-polarity, are markedly different from the typical low-amplitude, negative-polarity spikes usually seen in extracellular recordings. Intermittent spikes with amplitudes of 1 to 2 millivolts persisted for a duration of one minute. Consecutive spikes on top of a prolonged depolarization, similar to the typical shape of neuronal bursting activity,[3] were also clearly observed in the waveforms as shown in the magnified waveforms in subset figures (i) and (ii) in Figure 2a. The spikes, with amplitudes of a few millivolts and positive-polarity, typical of quasi-intracellular recordings[16,17] suggest that the signals captured by the nanowires are quasi-intracellular recordings from neurons in an intact brain.

The spiking events, spatially mapped onto the geometric structure of FINE, are shown in Figure 2b. The nanowire channels, labeled from f1 to f25, display the corresponding waveforms shown in black, while the planar contact waveforms, labeled from e1 to e18, are shown in blue. The nanowire channels recorded spikes with amplitudes as high as 5 mV whereas the planar contacts exhibited low sub-millivolt potentials typical for extracellular recordings. Several nanowires showed positive-polarity spikes (f1, f3, and f5), while other nanowires show negative-polarity spikes with lower amplitudes (f7, f11, and f13). Nanowires exhibiting positive-polarity spikes are most likely accessing the intracellular medium of neurons or may also be in direct contact with the neuronal cell membrane, whereas those showing negative-polarity spikes are likely recording from the extracellular medium. A similar observation of spatial variability in waveform polarity and amplitude recorded from single neurons was made using high-density microelectrode arrays, with neighboring channels spaced a few micrometers apart.[18] We speculate that nanowires f1, f3, and f5 had likely formed an intracellular interface with the recorded neurons, whereas f7, f11, and f13 nanowires were positioned with a small intervening gap with neurons yet still capable of effectively recording high-amplitude extracellular neuronal potentials from its nanoscale tip. The nanowire channels of FINE inside the intact brain were capable of consistently exhibiting spiking events for the duration of a single recording session of 10 min (Figure 2c), as demonstrated in a separate recording session (FINE 2). Throughout the 10 min recording session, we observed positive spikes with an amplitude up to 5 mV together with the lower frequency local field potentials. The recorded spike amplitude varied during the recording session, indicating variability in the interface geometry between the cell and the nanowires. The variability in the recorded spiking amplitude is consistent with that observed in vitro from neurons[8,19] and cardiomyocytes.[20–22] Similar

Figure 1. Fishbone intracellular nanowire electrode (FINE) concept, structural and electrical properties. a) Exploded view structure of FINE. Conceptual illustration of b) FINE inserted inside the cortex of the juvenile rat and c) the internalization mechanism of nanowire into the neuron. Cortical neurons image edited and reprinted with permission from H. Markram et al., Cell 163, 456–492 (2015). Copyright 2015 Elsevier. d) Optical microscope and e) SEM images of microfabricated FINE. f) X-ray diffraction characterization of PtSi before and after thermal annealing at 350 °C. g) Mechanical characteristics and h) electrical conductivity of Pt, amorphous and polycrystalline PtSi. i) TEM characterization of FINE; Bright field TEM, HR-TEM (inset), and diffraction pattern of *poly*-PtSi nanowire.

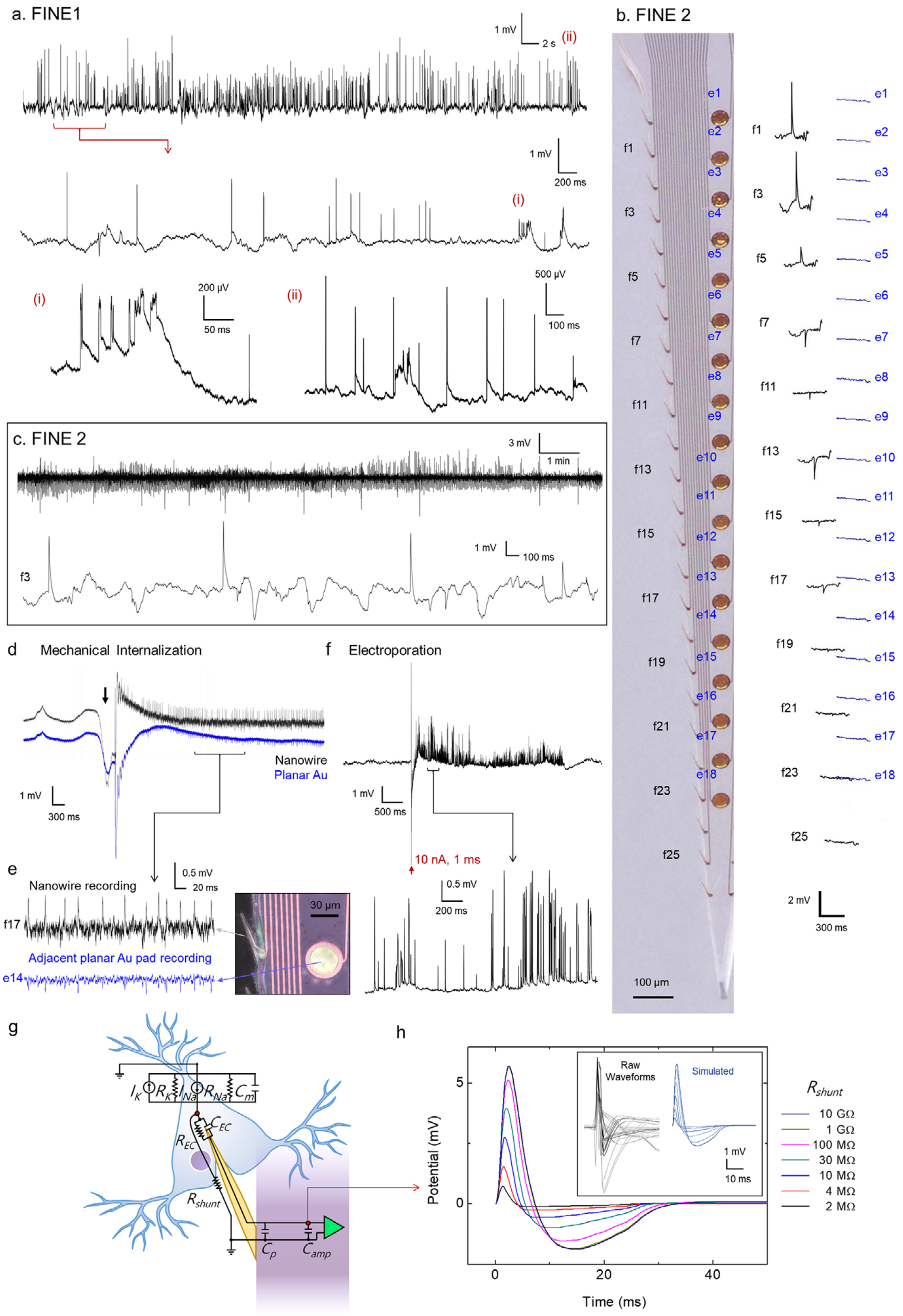

Figure 2. Quasi-intracellular recording from single shank FINE. a) Representative quasi-intracellular recording from FINE near the rat barrel cortex. Top trace is a 60 s long recording and bottom trace is 6 s long recording. The representative bursting neural activities are shown in detail in (i) and (ii) (Rat #11). b) Spatial mapping of recorded waveforms from nanowires versus extracellular planar contacts on FINE (Rat #8). c) Longer-term 10 min recording of FINE (Rat #8). d) Natural or mechanical internalization of nanowires into the neurons. e) Comparison of same neural signals simultaneously captures with nanowire channels and extracellular pads (Rat #8). f) Electroporation-based internalization mechanisms of nanowire into the neuron (Rat #11). g) Circuit diagram depicting the electrochemical interface of a nanowire on FINE penetrating a neuron. h) Simulated action potential at the input of the amplifier as a function of the sealing resistance, R_{shunt}. The inset figure shows the comparison between the raw recorded waveforms (Rat #7) and simulated waveforms. Results of (d) are presented from one of two rats with multishank FINE recordings (Rat #3). Results are presented from two of three rats that underwent single shank FINE recordings (Rats #11 and #8).

quasi-intracellular recordings were observed in different animal cases, as shown by the spatial mapping and waterfall plots presented in Figure S6 (Supporting Information).

We investigated the principal mechanism underlying the internalization of nanowires into neurons in the intact brain by analyzing the critical time points at which recordings from the nanowires shifted abruptly from negative to positive recordings. We interpret this shift as indicating a shift from extracellular to quasi-intracellular recordings. In most cases, after the mechanical movement of FINE was completed, nanowire recordings spontaneously transitioned into quais-intracellular recordings instantaneously or within a few seconds. As shown in Figure 2d, even in the absence of deliberate motion control of FINE, the nanowire recording shifted to quasi-intracellular recordings after a one-time substantial low-frequency potential deflection, which was likely caused by motional artifacts as this deflection was observed across all channels. This quasi-intracellular recording persisted for 10 min for nine nanowires in the same device (Figures S7 and S8, Supporting Information). These motion artifacts are potentially associated with either cerebral blood flow, breathing,[23] or external mechanical vibrations that could affect the mechanical interface between the nanowire and neurons. In another case, the deliberate retraction movement of FINE initiated the transition from extracellular to quasi-intracellular recording (see Figure S9, Supporting Information). In interpreting the data, we distinguished neuronal spikes from mechanically induced artifacts using both their spatial distribution and waveform characteristics. Mechanical artifacts typically appeared as synchronized, large-amplitude deflections across all channels with broad, slower waveforms, in contrast to the localized, sharp transients characteristic of true neuronal spikes, as exemplified in Figure 2d.

It is noteworthy that we observed in this recording that nanowire channels exhibited regular positive spikes whereas the adjacent planar Au contacts displayed time-locked and much smaller negative-polarity spikes (see Figure 2e). To assess whether the quasi-intracellular and extracellular signals originated from the same neuron, we evaluated synchrony using the spike time tiling coefficient (STTC)[24] and wavelet coherence analysis.[25] Spike times were extracted from a 20-second segment of data, and synchrony was then quantified using a 1 ms coincidence window. The resulting STTC value was 0.9, indicating a strong temporal correlation. In addition, wavelet coherence analysis revealed high coherence near 1 kHz (see Figure S10, Supporting Information). Together, these quantitative results provide compelling evidence that both the nanowire and the adjacent planar Au contacts recorded the same or simultaneously firing neurons. Due to the relatively large separation between the planar pads and nanowires, ranging from 100 μm (between f23 and e18) to 300 μm (between f1 and e1), simultaneous recordings of the same neuron by both nanowires and planar pads are expected to be less frequent.

Another method that enabled the nanowire electrodes to record quasi-intracellular potentials involved delivering a short biphasic, monopolar pulse (10 nA, 1 ms) to the sharp nanowire tip to electroporate the neuronal cell membrane.[7] Following a large-amplitude, slowly-decaying stimulation artifact, trains of spikes abruptly emerged on the recordings (Figure 2f) and lasted for ≈3 s. These spikes gradually decreased in amplitude before disappearing (see Figure 2f), a behavior consistent with the in vitro electroporation-based quasi-intracellular nanowire recording of cells.[19,26] This observation suggests that the electroporation of the nanowire-neuron interface, commonly utilized in vitro for nanowire microelectrode arrays, can be adapted for intact brain experimental setups. Further comparison of the signals obtained from natural internalization and electroporation-enabled nanowire–cell interfaces is presented in Figure S11 (Supporting Information).

We evaluated whether the neuron remained viable following extended quasi-intracellular recording via natural internalization (Figure S11, Supporting Information). In this case, a spontaneously formed intracellular-like signal persisted for 87 s before returning to baseline. After 30 s, a brief electrical pulse applied via electroporation momentarily re-established quasi-intracellular access. This recovery suggests that the neuron remained viable after the initial recording and that the nanowire maintained close proximity to the cell, allowing the interface to be reformed. These findings indicate the potential for non-destructive interfacing through natural internalization.

We examined the degree of signal distortion in the recorded potential relative to the actual potential at each nanowire tip, considering the nature of the nanowire-neuron interface configuration (see Figure 2g). When measuring potentials using electrophysiological systems configured for extracellular recordings, compensation for parasitic capacitances is not possible. Additionally, the dynamic range of the extracellular amplifiers are limited to ±6.4 mV, and the amplifier's bandwidth of 0.1 Hz to 7.5 kHz inherently prevents the measurement of DC resting membrane potentials (Intan Technologies, Inc.). Therefore, the recorded potentials of the nanowires differ from those recorded by patch-clamp and are heavily impacted by the nanowires' high-impedance, parasitic capacitance, and the specifics of the mechanically ruptured neuronal membrane around the nanowire. In prior in vitro studies on nanowire-neuron interfaces, we[8,15] and others[19,27] built on the Spira model[7,28,29] – despite the challenges of recording intracellular signals using multichannel extracellular recording amplifiers – investigated the impact of these effects on the temporal characteristics and amplitude of the recorded intracellular potentials with nanowires by circuit modeling as depicted in Figure 2g. Briefly, our model incorporates the membrane capacitance C_m and ion-specific membrane resistance R_{K}, R_{Na} along with their corresponding ionic currents I_K, I_{Na}. The electrochemical interface between the intracellular fluid and each nanowire was modeled as a simple Randles Cell which is composed of a parallel RC circuit (R_{EC}, C_{EC}). The quality of the membrane seal around the nanowire was modeled with a seal resistance, R_{shunt}. Using action potentials with a peak-to-peak amplitude of 100 mV obtained from whole-cell recordings, we simulated the amplitude and temporal distortion of action potentials measured by nanowires for a range of R_{shunt} from 1 MΩ (corresponding to a poor seal) to over 1 GΩ (corresponding to a near-perfect seal) (Figure 2h). All parameters used in the simulations are listed in Table S1 (Supporting Information). The simulations resulted in peak-to-peak amplitudes of the waveforms at the amplifier input ranging from 0.5 to 8 mV. The consistency between the measured amplitudes and full width half maximum (FWHM) of the potentials recorded with nanowires in FINE and those predicted by the model (inset figure in Figure 2h) suggests that the nanowire tips are accessing the intracellular medium of the cells.

2.3. Volumetric Quasi-Intracellular Recording with Scalable, High-Channel Count FINE

The FINE device was fabricated utilizing a scalable 6-inch wafer process, enabling the expansion to include several hundred nanowire channels and planar electrodes (see Figure S12, Supporting Information). This scaling was achieved through the replication of shanks and assembly into stacked, 3D multishank arrays, as depicted in **Figure** 3a. The electrode layout for each shank in the multishank array is identical to that of the single shank FINE depicted in Figures 1 and 2. The design features a fork-like structure with eight shanks, each spaced 500 µm apart, organized into three stacked layers separated by 1 mm spacers. When inserted into the brain, the recording volume is 4 mm (length) × 3 mm (width) × 2 mm (depth). Connections between the electrodes and the neural signal acquisition electronics were managed through a custom 1024-channel recording system.[30] The multishank FINE includes 594 nanowire channels and 430 planar Au recording sites. We recorded electrophysiological activity from these 1024 channels from the rat cortex. We classified quasi-intracellular potentials with the following criteria: i) a positive-polarity peak amplitude exceeding 0.5 mV, ii) a full width at half maximum (FWHM) of less than 5 ms, and iii) a signal-to-noise ratio (SNR) for the spike root-mean-square (RMS) amplitude to pre-spike background potentials greater than 5. The amplitude threshold for detecting quasi-intracellular potentials was determined from prior studies of in vitro interfaces between ultra-sharp nanowires and neurons, where individual nanowires recorded quasi-intracellular peak-to-peak potentials ranging from 0.5 to 12 mV.[31] The FWHM criterion of less than 5 ms was established based on the modeling results shown in Figure 2g,h.

We initially applied our spike detection method to single shank cases and observed quasi-intracellular potentials in 11 of 14 nanowire channels over a 2-h recording period (Figure 3b). Representative waveforms from each channel overlaid on top of each other are shown in Figure 3b. The signal-to-noise ratio (SNR) was calculated to be 32 ± 30, with a maximum SNR of 132. We then repeated the process for the multishank FINE. During a 1-h recording session, quasi-intracellular potentials were detected on 127 of 594 nanowire channels. The probability of recording quasi-intracellular spikes from the multishank FINE was reduced compared to the single shank FINE because of the increased invasiveness and bleeding that accompanied the insertion of the multishank FINE into the rat cortex (Figure S12g, Supporting Information). This also resulted in a reduced SNR for the multishank FINE compared to the single-shank version, with an average of 16 ± 10 and a maximum SNR of 81. Representative spike waveforms collected from these channels are overlaid on top of each other in Figure 3c. This multishank FINE array incorporated various combinations of nanowire lengths and deflection angles across the 24 shanks within a single device (Figure S13, Supporting Information); however, for this particular case, no observable differences in the likelihood of achieving intracellular-like recordings were noted across the different shank configurations.

The histogram of spike-like waveforms identified solely by the 300 µV threshold during the 1 h session exhibited peak-to-peak amplitudes centered ≈1 mV with a tail extending up to 12 mV as illustrated in Figure 3d. The histogram of FWHM peaks, also shown in Figure 3d ranged from 1 to 80 ms. Our quasi-intracellular spike detection criteria used to generate Figure 3b,c only selected those that simultaneously had i) over 0.5 mV amplitude and ii) less than 5 ms FWHM, which are colored in red in the histograms of Figure 3d.

To investigate the spatial distribution of quasi-intracellular potentials, we overlaid representative waveforms from each nanowire on a probe map (Figure 3e). The waveforms are colored in black, blue, and red for the 1st, 2nd, and 3rd layers of multishank FINE, respectively. The large-amplitude intracellular spikes were observed across many different nanowire channels distributed across multiple positions within the brain. In specific regions, adjacent nanowire channels exhibited quasi-intracellular potentials more frequently than others, either due to the large recording span over multiple barrel cortices or due to elective proximity to neurons in particular regions with reduced trauma due to implantation. Similar recording results can be found from another earlier rat case with multishank FINE (Figure S14, Supporting Information).

The 3D quasi-intracellular recording presents an opportunity to investigate the spatiotemporal relationship between spikes. Typical raw recording traces from the 594 nanowire channels are displayed in a waterfall plot in Figure 3f, with additional traces from both single shank and multishank FINE shown in Figure S15 (Supporting Information). Given that the spike-like waveforms typically precede or follow each other in the waterfall plots, we constructed a raster plot (Figure 3g). This plot includes all spikes from the histogram in Figure 3d, detected using a relatively relaxed spike-sorting criteria, to demonstrate the potential of quasi-intracellular recordings from multiple neurons across the volume of tissue surrounding multi-shank FINE. The raster plot enables visualization of each spiking event as a short vertical line, scattered across various time points and channel numbers. Using the spike occurrence time, we constructed an artificial 3D landscape and computed the spatial gradient to derive a vector map. We then utilized a streamline technique as a visual aid to illustrate the spatiotemporal dynamics of spikes in Figure 3h. The streamlines were color-coded according to the timing of their origin from the preceding spike. Blue streamlines delineate the earliest occurring spikes and their spatiotemporal progression toward the subsequent spikes, whereas green, yellow, and red streamlines represent the following spikes. Though the spikes for this plot were not restricted to quasi-intracellular activity spikes, this proof-of-concept, color-coded streamline plot could offer insights into the spatial connectivity patterns among the volumetrically distributed spikes.

Our results show that nanowires are capable of recording quasi-intracellular spikes together with low frequency local field potentials (LFPs) that are coupled through partial exposure of the nanowire to the extracellular medium. Quasi-intracellular potentials are evident from the raw recording traces from the nanowire channels in FINE displayed in waterfall plots in Figure 3f and Figure S9 (Supporting Information), where the potentials were measured with respect to the reference needle positioned on the clavotrapezius muscle near the neck. Leveraging the broadband

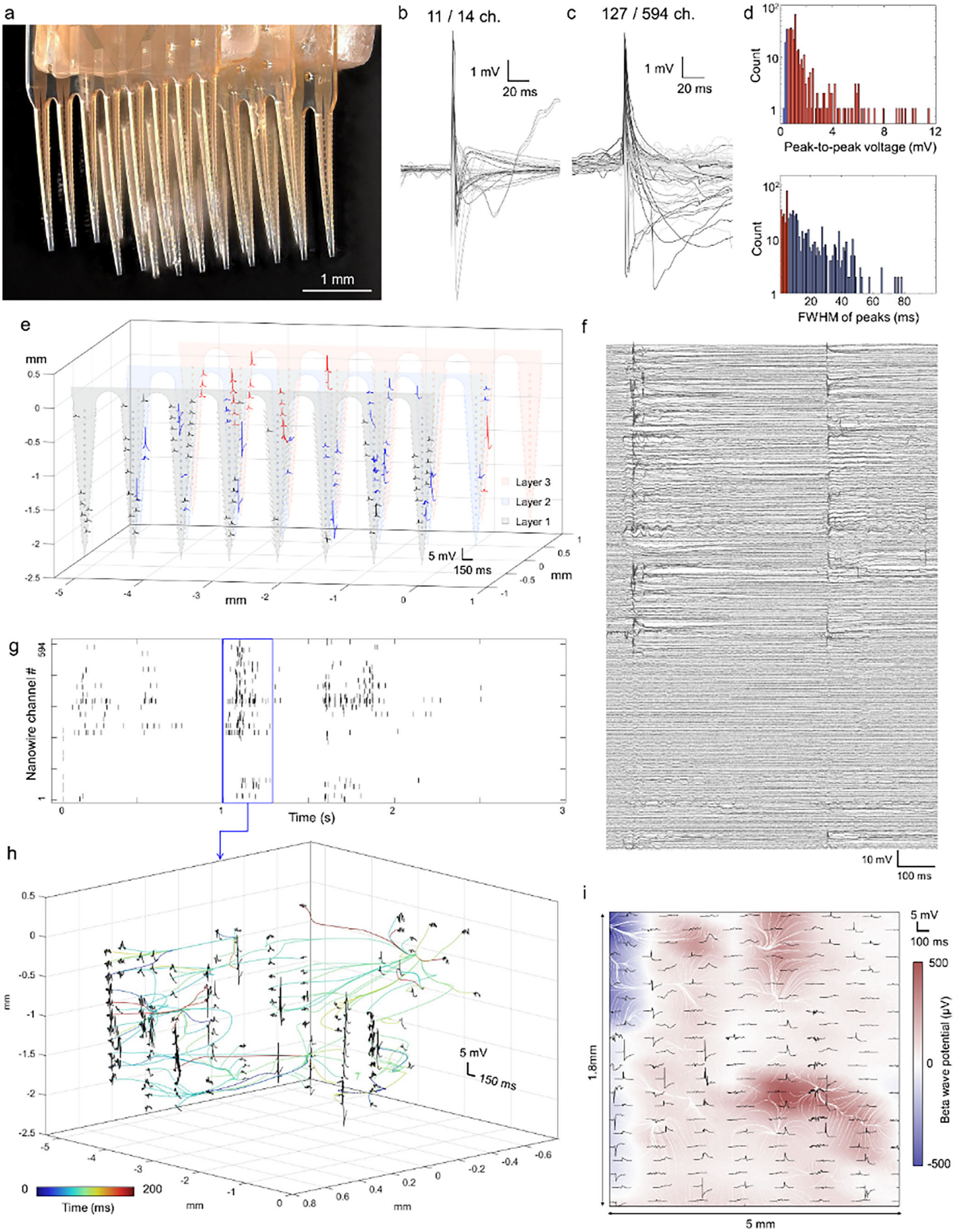
a
1 mm
b
11 / 14 ch.
1 mV
20 ms
c
127 / 594 ch.
1 mV
20 ms
d
Count
Peak-to-peak voltage (mV)
Count
FWHM of peaks (ms)
e
mm
Layer 3
Layer 2
Layer 1
5 mV
150 ms
mm
mm
f
10 mV
100 ms
g
Nanowire channel #
594
1
Time (s)
h
mm
5 mV
150 ms
Time (ms)
0
200
mm
mm
i
1.8mm
5 mm
5 mV
100 ms
Beta wave potential (μV)
500
0
-500

recording capability of nanowire channels, we constructed a plot correlating the propagation dynamics of beta waves with quasi-intracellular spiking activity from nanowires distributed across eight shanks on a single plane (Figure 3i). In the foreground, the waveforms of nanowire channels, some of which exhibited quasi-intracellular potentials, are spatially distributed atop the positions of the nanowire channels. In the background, the potential map of the beta wave (9–18 Hz) detected from the nanowire electrodes is plotted together with white streamlines depicting the propagation dynamics of the beta waves, calculated through phase gradient analysis.[32] These data illustrate how nanowire channels, equipped with broadband neural signal recording capabilities, can facilitate measurement and visualization of intricate neural dynamics by correlating conventional LFPs with quasi-intracellular potentials across multiple channels for a given planar cut of the 3D FINE recording.

2.4. Optical Imaging of FINE Implanted within the Brain

To visualize the spatial relationship between FINE nanowires and neurons in vivo, we utilized an optical clearing technique using EZ-CLEAR, followed by Neurotrace (Nissl) staining and fluorescence microscopy imaging.[33] The fluorescence microscope image in **Figure 4a** displays the FINE (red, autofluorescence) after implantation, surrounded by cells (Neurotrace, green) within the brain. To minimize potential movements of the FINE during tissue preparation for EZ-CLEAR imaging, we inserted the FINE after perfusion fixation specifically for this imaging experiment. In this configuration, the nanowires on the FINE are expected to experience increased mechanical resistance against the fixed brain tissue, as the fixation process is known to enhance the turgor of the brain.[34] Most of the nanowires remained straight and extended from the shank toward the nearby neuronal cell bodies, demonstrating structural integrity despite the increased turgor of the fixed brain tissue. Given that FINE maintained its structural integrity in the stiffer fixated brain tissue, the nanowires are expected to remain intact under the lower mechanical stress of the softer intact brain. A further magnified image in Figure 4b,c provides a closer look at the nanowire-neuron interface. The FINE's nanowires had neurons positioned very close to their tips, with the size of each nanowire tip allowing for the probing of one neuron at a time. Given the blind insertion nature of the FINEs, we do not have the ability to precisely control alignment of the nanowires with the neurons. Nonetheless, there is a considerable likelihood that the tips of the nanowires will establish contact with the neuronal cell bodies. This assumption is based on the fact that cell bodies provide a much larger volume and surface area for nanowire contact compared to subcellular structures such as dendrites. However, dendritic recordings may also occur if the nanowire tips happen to align with dendritic branches during insertion. To accurately identify the subcellular recording site, it will be necessary to further develop FINE to be compatible with advanced optical techniques, such as two-photon microscopy combined with fluorescent labeling capable of in vivo deep-tissue imaging at subcellular resolution. The side-view image of the FINE in Figure 4d,e further illustrate how the nanowires (red) are oriented within the tissue. The side view image suggests that the nanowires implanted into the fixated brain were slightly bent, forming a hook-like structure. This hook-like, elastic structure of the nanowires could be advantageous in minimizing damage during insertion and for effective probing of neurons.

The engineered PtSi nanowires were tailored to enhance hardness and are sufficiently robust to endure the implantation process within the brain. Furthermore, their elasticity enabled them to spring back inside the brain tissue to intimately interact with surrounding neurons. More importantly, we were able to further control the hardness, elasticity, and conductivity of *poly*-PtSi nanowires by adjusting the alloy composition and annealing conditions. These adjustments allowed us to fine-tune the mechanical and electrical properties of the nanowires, further optimizing them for in vivo quasi-intracellular recording.

3. Discussion

The development and implementation of FINE represents a substantial engineering leap in the pursuit of recording intracellular potentials in 3D within intact brains. Our findings highlight that FINE can record quasi-intracellular potentials across numerous channels deep within an intact brain which has historically posed significant engineering challenges for other neural recording techniques. The advances described here also resemble a substantial leap for nanowire technologies, as prior nanowire techniques are limited to in vitro studies. The unique fishbone architecture not only facilitates the robust delivery of the nanowires within the intact brain but also enables sustained high-fidelity intracellular recordings.

We have shown that FINE can record quasi-intracellular spikes with higher amplitude and SNR compared to conventional planar recording contacts which have only recorded extracellular potentials to date. This advanced electrophysiology recording capability enables more detailed analysis of neuronal activity than was previously possible and has the potential to expand our understanding of the brain function. The successful scaling of this technology through the development of a 24-shank array system underscores FINE's potential to explore and map complex neural networks across various brain regions simultaneously. The promising results demonstrated by FINE could potentially revolutionize intracellular recording practices in neuroscience research. By enabling detailed and scalable recordings from deep

Figure 3. Volumetric quasi-intracellular recording from multi-shank FINE. a) Photo of 24 multishank FINE with 594 channels nanowires and 430 extracellular electrodes. Representative quasi-intracellular spikes from different channels overlaid on top of each other where b) 11 of 14 nanowire channels showed quasi-intracellular potentials from single shank FINE (Rat #7) and c) 127 of 594 nanowire channels from multishanks FINE showed quasi-intracellular potentials (Rat #12). d) Histograms of amplitude and FWHM of overall spikes from a single recording session. e) Spatial distribution of representative quasi-intracellular spike waveforms. f) Waterfall plot of waveforms across 594 nanowire channels. g) Raster plot of spikes and corresponding h) spatial distribution of spikes together with streamlines representing the timing and spatiotemporal progression from the preceding to subsequent spikes. i) Simultaneous depiction of beta wave propagation represented with colormap and streamline overlaid with the spatial distribution of quasi-intracellular potentials. Results are presented from one of two rats that underwent multishank FINE recordings (Rat #12).

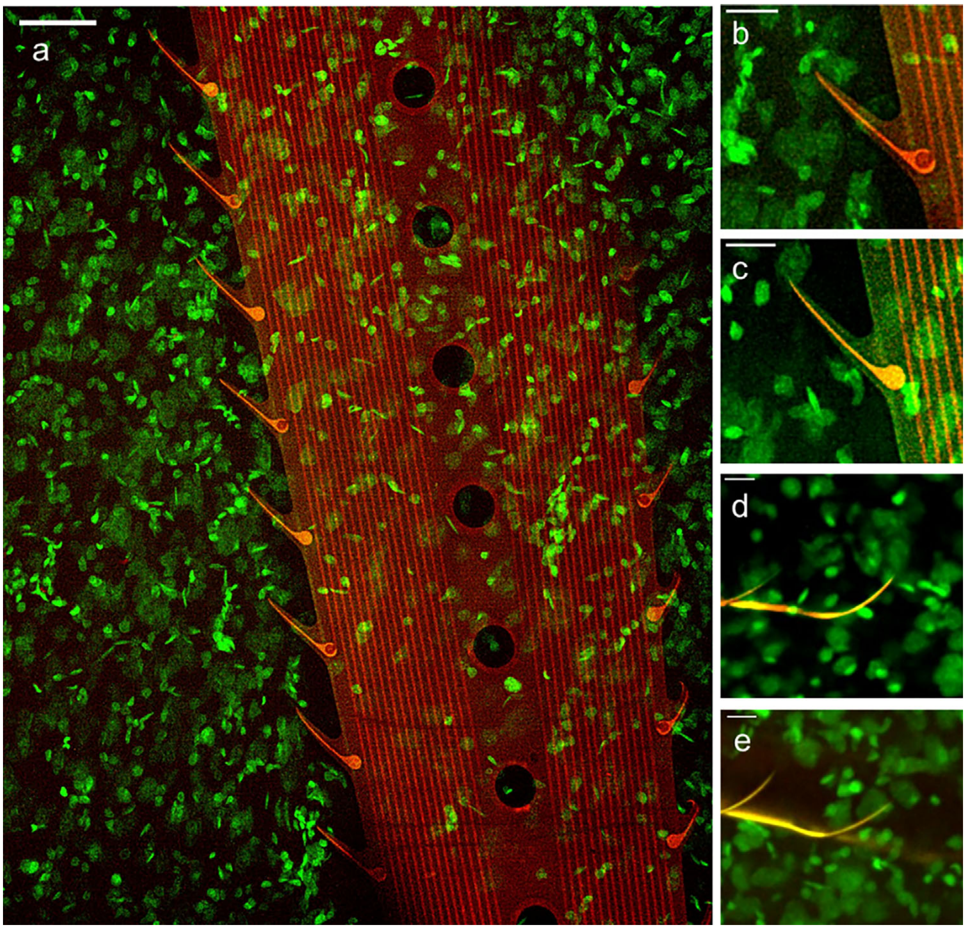

Figure 4. Optical image of FINE-brain interface. a) FINE (red) implanted into the cleared brain imaged together with the Nissl-stained cells (green; scale bar is 500 µm). Magnified views showing the proximity between the nanowires and the neuronal cell bodies in the b,c) top view and d,e) side view with respect to the electrode surface. Scale bars for (b–e) are 20 µm.

within intact brains, FINE opens new avenues for exploring the intricate dynamics of neural networks and their roles in cognitive functions and behaviors. This advancement in enhanced electrophysiological recording at the intracellular level with sensitivity to subthreshold potential oscillations (Figure 2) could also lead to breakthroughs in diagnosing and treating neurological disorders by providing deeper insights into their underlying neural mechanisms.

Despite its numerous advantages, the practical application of FINE in broader research and clinical settings requires further refinement. Due to the relatively large multi-shank FINE measuring 4 mm × 3 mm × 2 mm, the simultaneous insertion of all 24 shanks into the cortex resulted in extensive bleeding and trauma that limited the fidelity of the 3D quasi-intracellular recordings. While microscale advancements of the multi-shank FINE rarely resulted in motion artifacts, the appearance of similar spikes across many channels in one instance (Figure 3f) cannot be fully ruled out to be a motion artifact. This issue, however, was not observed in any other recordings performed by the authors. One plausible explanation for the observed synchrony is co-activation of neurons within the barrel cortex. As no additional contextual information beyond the neural signals was available in this session, the exact source of the synchrony remains uncertain. Incorporating sensory-evoked protocols, such as controlled whisker deflection, could help distinguish true neuronal co-activation from motion-related artifacts and represent a valuable direction for future studies. Additionally, simultaneous recordings with whole-cell patch-clamp would offer more rigorous validation of the signals captured at the nanowire interface. While multiple prior studies have already demonstrated simultaneous patch-clamp validation of intracellular-like signals using nanowire electrodes in vitro,[35,36] our work builds upon this foundation by demonstrating the in *vivo* application of nanowires in an intact brain. In future studies, it would be valuable to incorporate approaches such as targeted in vivo patch-clamp to further validate and characterize the nanowire-neuron interface under physiological conditions.[37] While FINE demonstrated sensitivity to subthreshold activity, the current study did not include pharmacological or circuit-level validation. As future work, we propose targeted implantation combined with stimulation and recording of connected neuronal populations to validate the synaptic origin of subthreshold signals with FINE. Moreover, it would be crucial to record the absolute membrane potential with nanowires that undergo reversible Faradaic interactions with the cytoplasm. This is typically accomplished with a Ag/AgCl electrode that can reach equilibrium with the cytoplasm potential and instantaneously respond to its changes. Such nanowires may be fabricated in the FINE architecture with a Ag containing alloy with Si followed by a Ag/AgCl coating/chlorination or by applying this Ag/AgCl coating to a PtSi nanowire thereby preserving the structural integrity and enabling the recording capability of the absolute membrane potential. Alongside the development of Faradaic-interface materials capable of supporting absolute membrane potential measurements, it will be essential to integrate such interfaces with a DC-coupled amplifier, as opposed to the AC-coupled system (Intan Technologies, Inc.) employed in this study. While the 10-minute duration of continuous quasi-intracellular recording is already notable given the complexity of the in vivo environment, this limitation appears primarily due to mechanical disturbances from the periodic administration of Ketamine/Xylazine anesthesia, required every 15 min. Despite careful hindlimb injections to minimize movement, these interventions introduced subtle motion that could disrupt the delicate nanowire-neuron interface. Developing a mechanically stable IV anesthesia protocol would be valuable for extending recording duration. Additionally, intrinsic brain dynamics, such as pulsatile brain motion,[38] likely contribute to signal instability. These challenges become even more pronounced in freely moving animals, where larger-scale motion can further destabilize the nanowire-neuron interface. To solve this issue, we envision that the fishbone architecture employed on less invasive, soft and stretchable shanks and potentially implanted one at a time[39] could enhance mechanical stability of the nanowire-neuron interface within brain tissue while also reducing trauma and biofouling for chronic recordings from freely moving animals. To better evaluate the recording site and potential subcellular damage, future studies should integrate FINE with high-resolution in vivo imaging techniques, such as two-photon microscopy combined with fluorescent labeling. While Figure 4 shows intact nanowires near neuronal somata, the current staining method did not allow assessment of axonal or dendritic disruption. As FINE evolves into a high-precision scientific tool, minimizing subcellular damage and visualizing fine-scale probing sites will become increasingly important. Although this study conceptually demonstrated the feasibility of FINE for quasi-intracellular recording, further systematic optimization of its structural parameters will be important to maximize recording efficiency while minimizing tissue damage. As the architecture of FINE and physical properties of engineered nanowires continue to be improved, the prospects for widespread adoption and impactful contributions of this nanowire-integrated neural probe technology in the field of neuroscience remains exceptionally promising.

4. Experimental Section

Nanofabrication of FINE: The fabrication process of FINE utilized a 6-inch silicon (Si) wafer. Initially, the wafer was activated using O_2 plasma treatment, followed by the application of an anti-adhesion Micro90 solution. Subsequently, a diluted PI2611:NMP (1:1) solution was spin-coated onto the wafer to form a polyimide layer with a thickness of 700 nm. Ti hard mask (20 nm) was formed on the initial polyimide layer through standard photolithography, e-beam evaporation, and lift-off processes, serving as a component in the final fabrication step for patterning the polymer layer via a plasma etching step to define the passivation layers of nanowires, planar extracellular recording sites, and contact pads to interconnect with the electrophysiological recording systems. Subsequently, a second polyimide layer with a thickness of 700 nm was deposited, covering the 1st polyimide and Ti hard mask. Metal leads with both the width and spacing of 3 µm were fabricated through a series of standard maskless photolithography, e-beam evaporation of Cr/Au (10/250 nm), and lift-off processes.

Following the deposition of metal leads, planar PtSi nanowires were formed on the terminal sites of the metal leads by e-beam lithography EBL), sequentially stacking or co-sputtering Pt and Si thin films, and lift-off process. For the sequentially stacked Pt and Si films, the thickness profile was 5/80/80/160/80/80/5 nm of Cr/Pt/Si/Pt/Si/Pt/Cr. The amorphous was transformed, as-deposited PtSi into polycrystalline PtSi by thermally annealing the structure at 350 °C for 10 min under N_2 atmosphere. Metal leads and PtSi nanowires were coated with parylene C layer (700 nm) after an O_2 plasma treatment (200 W, 30 s). Ti hard mask was formed and polymer layers were etched by O_2 reactive ion etching (RIE) to define the shank structure as well as the passivation layers of nanowires that covers most of the nanowires' main bodies but expose only their final 2 µm tip portion.

A SU-8 polymer shank (50 µm) was added on top by standard photolithography process, and the entire structures were lifted off from the underlying Si wafer by combination of XeF_2 etching of Si and immersion of the wafer in DI water that dissolved the Micro90 layer, releasing the FINE from the Si wafer. After the lift-off, the flexible polymer layers were flipped upside down and O_2 RIE (100 W, 10 min) first etched away the 1st polyimide layer, and patterned the 2nd polyimide layer through the pre-deposited Ti hard mask to expose the planar recording sites and interconnection pads. This process also defined the sophisticated passivation layers around the nanowires by etching away the polymers that were underneath the nanowire tips.

Material Characterization: Morphology analysis was performed by scanning electron microscope (SEM, Apreo; FEI). For detailed microstructural analysis, the *poly*-PtSi nanowires on FINE were examined using transmission electron microscopy (TEM, Talos F200X G2; Thermofisher). To image under TEM the probes site of FINE was trimmed and attached on a lacey carbon coated TEM grids using a silver epoxy (8331D, MG chemicals) as an adhesive. Furthermore, the crystallinity of the *poly*-PtSi nanowires was investigated using high-resolution (HR) TEM and diffraction pattern (DP). The formation of *poly*-PtSi through thermal annealing process was characterized using X-ray diffraction (XRD, SmartLab; Rigaku) θ-2θ scan. The sheet resistance was measured using a six-point probe measurement system.

Animal Experiments: All procedures for the rat experiment were approved by the UCSD Institutional Animal Care and Use Committee under protocol S16020. Male Sprague Dawley Rats (10-18 weeks of age, 300–600 g) from Charles River were sedated with 3–4% isoflurane and fixed in a stereotaxic frame (Kopf Instruments). A craniotomy was made by either exposing the somatosensory cortex or cerebellum. The dura was carefully removed. Once the craniotomy was complete, the rat was transitioned from isoflurane to ketamine/xylazine (100 mg kg^{-1} ketamine/10 mg kg^{-1} xylazine) and re-dosed every 15–30 min for the duration of the experiment. Temperature, heart rate, and oxygen concentrations were monitored for the entirety of the experiment to ensure adequate anesthesia.

A single-shank FINE, equipped with 25 nanowires and 18 planar contacts, was gradually inserted from its tip into the barrel cortex or cerebellum. The insertion was controlled at a steady advancement speed ranging from 2 to 10 µm s^{-1}, utilizing a motorized linear actuator system (IST motor, NeuroNexus). After fully inserting FINE into the cortex, the waveforms were monitored from the nanowire channels displayed in real-time. In the initial animal experiment (Rat #3, Figure S7, Supporting Information), intracellular-like signals emerged spontaneously within ≈30 s after full insertion to the target depth, following a brief motion artifact. In a subsequent case (Rat #7, Figure S9, Supporting Information), intracellular-like activity did not appear immediately after insertion but was reliably triggered by fine, deliberate mechanical adjustments of the probe. Based on these observations, a refined insertion protocol was implemented from Rat #7 onward, in which controlled micromovements were systematically applied to promote stable nanowire–neuron interfacing. This approach consistently increased the likelihood of achieving quasi-intracellular recordings across multiple channels.

As FINE probes were made of delicate nanowire arrays, they were designed for single-use applications. None of the probes were reused to avoid potential structural degradation or biomaterial accumulation after an explanation that could compromise the quality of subsequent recordings. Data acquisition was not blinded, and no randomization was applied in subject selection. No statistical tests were conducted, as the study was designed to qualitatively evaluate the feasibility of using the FINE to record intracellular-like potentials in intact brain tissue.

Signal Recording and Processing: Neuronal electrical activity was recorded using the FINE system interfaced with either an Intan RHD recording system or an Intan RHS stimulation and recording system (Intan Technologies). For multishank FINE devices, a custom-designed printed circuit board populated with sixteen RHD2164 chips (Intan Technologies) was used to interface with 1024 recording channels. Signals were sampled at 20–30 kHz per channel with a bandwidth of 0.1 Hz to 7.5 kHz. Recordings were initiated prior to probe insertion and continued throughout the implantation procedure. Real-time monitoring of signal amplitude was used to guide submicron-scale positional adjustments during insertion. For selected single-shank experiments, electroporation was performed using a short biphasic, monopolar current pulse (10 nA, 1 ms) delivered through the nanowire tip to transiently access the intracellular environment.

Raw voltage traces were exported and processed offline using MATLAB R2023a (MathWorks). To preserve broadband activity, including intracellular-like spikes and subthreshold signals, only a 60 Hz notch filter was applied for noise reduction. Recording segments affected by external noise, including motion artifacts or high levels of electromagnetic interference, were excluded from the analysis. High-amplitude spikes were identified using both amplitude thresholding and full-width-at-half-maximum (FWHM) criteria. Signal-to-noise ratio (SNR) was calculated as the ratio of peak spike amplitude to the root-mean-square (RMS) of the baseline noise prior to the onset of spiking activity. To visualize spiking activity, raster plots were generated, with each spike represented as a vertical line corresponding to its time and channel location. Using spike occurrence times and spatial mapping data, a 3D gradient of the spike timing landscape was computed to generate a vector field. This vector field was used to construct streamlines representing spatiotemporal propagation patterns of neural activity. Streamlines were color-coded according to the relative timing of each spike within a sequence. To assess synchrony and coherence between adjacent nanowire and extracellular channels, spike time tiling coefficient (STTC) and wavelet coherence analysis were performed.

Brain Clearing and Imaging: Following perfusion with 4% paraformaldehyde (PFA), the brain was postfixed in 4% PFA overnight. The following day, FINE was inserted into the perfused brain, and the brain was roughly blocked into a ≈3 mm thick coronal section around FINE. The sectioned brain was washed 3 times in PBS for 90 min each, and stored in PBS overnight at 4 °C. Two days later, the tissue was placed in 50% tetrahydroflorane (v/v with ddH_2O) and left nutating at room temperature for 36 h. Then, the tissue was washed 4 times in PBS for 1 h each at room temperature and transferred to blocking solution (2% normal goat serum, 0.05% sodium azide, and 0.08% Triton-X in PBS) for 24 h. The brain was then transferred to blocking solution containing 1:200 Neurotrace 520/525 (ThermoFisher N21480) for 48 h. The brain underwent a final 12 h wash in PBS at RT, and was then transferred to EZ View solution.[33]

Following optical clearing, confocal images were acquired on an inverted Andor BC43 spinning disk confocal with a 50 µm pinhole disk. The system was equipped with four laser lines, 405, 488, 561, and 638. The camera was a 16 bit Andor 4.1MP sCMOS with 6.5 micron pixels. A 10x/0.45NA Plan Apo LD Air objective and laser lines at 488 and 561 were used. The system was driven by the Fusion software. Images were deconvolved using the ClearView algorithm in the Fusion software from Andor. The image was rendered using Imaris (Oxford Instruments), and maximum projection images were created using FIJI.

Supporting Information

Supporting Information is available from the Wiley Online Library or from the author.

Acknowledgements

The authors are grateful for the technical support from the nano3 cleanroom facilities at UC San Diego's Qualcomm Institute where the fabrication of the FINE was conducted. The authors are grateful to Samantha M. Russman and Grace Lykins for assistance in rat experiments, and Keundong Lee for nanofabrication process assistance. The authors acknowledge expert technical assistance by Brian Jenkins and Hannah Bronstein in the Oregon Health and Science University Advanced Light Microscopy shared resource (RRID:SCR_009961). This work was performed in part at the San Diego Nanotechnology Infrastructure (SDNI) of UC San Diego, a member of the National Nanotechnology Coordinated Infrastructure, which is supported by the National Science Foundation (Grant ECCS1542148).This work was supported by S.A.D.'s faculty startup package in part by the National Institutes of Health Award No. NIBIB DP2-EB029757 (to S.A.D.) and in part by the BRAIN® Initiative NIH grants R01NS123655 (to S.A.D.), K99NS119291 (to K.J.T.), UG3NS123723 (to S.A.D.), 5R01NS109553 (to E.H.), and in part by NRF of Korea RS-2024-00351532 (to Y.T.). Any opinions, findings, and conclusions or recommendations expressed in this material are those of the author(s) and do not necessarily reflect the views of the funding agencies.

Conflict of Interest

The authors declare the following competing financial interest(s): J.L., D.R.C., I.G., E.H., and S.A.D have shares in Cortical Science Inc. that licensed a patent disclosure related to this work. The other authors declare that they have no competing interests.

Data Availability Statement

The data that support the findings of this study are available from the corresponding author upon reasonable request.

Keywords

electrophysiology, intact brain, intracellular, nanowire, recording

Received: March 2, 2025
Revised: July 16, 2025
Published online:

---

[1] E. Neher, B. Sakmann, *Sci. Am.* **1992**, *266*, 44.
[2] D. Ogden, *Microelectrode Techniques. The Plymouth Workshop Handbook*, The Company of Biologists Ltd, Cambridge **1994**.
[3] M. A. Long, A. K. Lee, *Curr. Opin. Neurobiol.* **2012**, *22*, 34.
[4] H.-J. Suk, E. S. Boyden, I. van Welie, *J. Neurosci. Methods* **2019**, *326*, 108357.
[5] S. B. Kodandaramaiah, G. L. Holst, I. R. Wickersham, A. C. Singer, G. T. Franzesi, M. L. McKinnon, C. R. Forest, E. S. Boyden, *Nat. Protoc.* **2016**, *11*, 634.
[6] A. K. Lee, J. Epsztein, M. Brecht, *Nat. Protoc.* **2009**, *4*, 385.
[7] A. Hai, M. E. Spira, *Lab Chip* **2012**, *12*, 2865.
[8] R. Liu, J. Lee, Y. Tchoe, D. Pre, A. M. Bourhis, A. D'Antonio-Chronowska, G. Robin, S. H. Lee, Y. G. Ro, R. Vatsyayan, K. J.

Tonsfeldt, L. A. Hossain, M. L. Phipps, J. Yoo, J. Nogan, J. S. Martinez, K. A. Frazer, A. G. Bang, S. A. Dayeh, *Adv. Funct. Mater.* **2022**, *32*, 2108378.
- [9] W. Hällström, T. Mårtensson, C. Prinz, P. Gustavsson, L. Montelius, L. Samuelson, M. Kanje, *Nano Lett.* **2007**, *7*, 2960.
- [10] C. Xie, J. Liu, T.-M. Fu, X. Dai, W. Zhou, C. M. Lieber, *Nat. Mater.* **2015**, *14*, 1286.
- [11] T. Chu, C. Ho, *Therm. Conduct.* **1978**, *15*, 79.
- [12] P. Chapman, O. Tufte, J. D. Zook, D. Long, *J. Appl. Phys. Sci.* **1963**, *34*, 3291.
- [13] M. Auslender, S. Hava, *Springer Handbook of Electronic and Photonic Materials*, 2nd ed., Springer, Cham **2017**, p. 1.
- [14] Y. Tchoe, J. Lee, R. Liu, A. M. Bourhis, R. Vatsyayan, K. J. Tonsfeldt, S. A. Dayeh, *Appl. Phys. Rev.* **2021**, *8*, 041317.
- [15] R. Liu, R. Chen, A. T. Elthakeb, S. H. Lee, S. Hinckley, M. L. Khraiche, J. Scott, D. Pre, Y. Hwang, A. Tanaka, Y. G. Ro, A. K. Matsushita, X. Dai, C. Soci, S. Biesmans, A. James, J. Nogan, K. L. Jungjohann, D. V. Pete, D. B. Webb, Y. Zou, A. G. Bang, S. A. Dayeh, *Nano Lett.* **2017**, *17*, 2757.
- [16] A. Coenen, A. Vendrik, *Exp. Brain Res.* **1972**, *14*, 227.
- [17] M. Y. Inyushin, V. Y. Tsytsarev, A. Y. Ignashchenkova, D. Lenkov, *Neurosci. Behav. Physiol.* **1997**, *27*, 702.
- [18] M. E. J. Obien, K. Deligkaris, T. Bullmann, D. J. Bakkum, U. Frey, *Front. Neurosci.* **2015**, *8*, 423.
- [19] C. Xie, Z. Lin, L. Hanson, Y. Cui, B. Cui, *Nat. Nanotechnol.* **2012**, *7*, 185.
- [20] J. Abbott, T. Ye, K. Krenek, L. Qin, Y. Kim, W. Wu, R. S. Gertner, H. Park, D. Ham, *IEEE J. Solid-State Circ.* **2020**, *55*, 2567.
- [21] Z. Jahed, Y. Yang, C.-T. Tsai, E. P. Foster, A. F. McGuire, H. Yang, A. Liu, C. Forro, Z. Yan, X. Jiang, M.-T. Zhao, W. Zhang, X. Li, T. Li, A. Pawlosky, J. C. Wu, B. Cui, *Nat. Commun.* **2022**, *13*, 2253.
- [22] B. Desbiolles, E. De Coulon, A. Bertsch, S. Rohr, P. Renaud, *Nano Lett.* **2019**, *19*, 6173.
- [23] T. P. Santisakultarm, N. R. Cornelius, N. Nishimura, A. I. Schafer, R. T. Silver, P. C. Doerschuk, W. L. Olbricht, C. B. Schaffer, *Am. J. Physiol.-Heart Circ. Physiol.* **2012**, *302*, H1367.
- [24] C. S. Cutts, S. J. Eglen, *J. Neurosci.* **2014**, *34*, 14288.
- [25] C. Arnal-Real, M. Mahmoudzadeh, M. Manoochehri, M. Nourhashemi, F. Wallois, *Front. Neurol.* **2021**, *12*, 596926.
- [26] J. Abbott, T. Ye, L. Qin, M. Jorgolli, R. S. Gertner, D. Ham, H. Park, *Nat. Nanotechnol.* **2017**, *12*, 460.
- [27] N. Shmoel, N. Rabieh, S. M. Ojovan, H. Erez, E. Maydan, M. E. Spira, *Sci. Rep.* **2016**, *6*, 27110.
- [28] A. Fendyur, N. Mazurski, J. Shappir, M. E. J. F. i. n Spira, *Front. Neuroeng.* **2011**, *4*, 14.
- [29] S. M. Ojovan, N. Rabieh, N. Shmoel, H. Erez, E. Maydan, A. Cohen, M. E. Spira, *Sci. Rep.* **2015**, *5*, 14100.
- [30] Y. Tchoe, A. M. Bourhis, D. R. Cleary, B. Stedelin, J. Lee, K. J. Tonsfeldt, E. C. Brown, D. A. Siler, A. C. Paulk, J. C. Yang, H. Oh, Y. G. Ro, K. Lee, S. M. Russman, M. Ganji, I. Galton, S. Ben-Haim, A. M. Raslan, S. A. Dayeh, *Sci. Transl. Med.* **2022**, *14*, abj1441.
- [31] R. Liu, J. Lee, Y. Tchoe, D. Pre, A. M. Bourhis, A. D'Antonio-Chronowska, G. Robin, S. H. Lee, Y. G. Ro, R. Vatsyayan, K. J. Tonsfeldt, L. A. Hossain, M. L. Phipps, J. Yoo, J. Nogan, J. S. Martinez, K. A. Frazer, A. G. Bang, S. A. Dayeh, *Adv. Funct. Mater.* **2022**, *32*, 2108378.
- [32] L. Muller, G. Piantoni, D. Koller, S. S. Cash, E. Halgren, T. J. Sejnowski, *Elife* **2016**, *5*, 17267.
- [33] C.-W. Hsu, J. Cerda, J. M. Kirk, W. D. Turner, T. L. Rasmussen, C. P. Flores Suarez, M. E. Dickinson, J. D. Wythe, *Elife* **2022**, *11*, 77419.
- [34] H. Metz, J. McElhaney, A. K. Ommaya, *J. Biomech.* **1970**, *3*, 453.
- [35] J. T. Robinson, M. Jorgolli, A. K. Shalek, M. H. Yoon, R. S. Gertner, H. Park, *Nat. Nanotechnol.* **2012**, *7*, 180.
- [36] Q. Qing, Z. Jiang, L. Xu, R. Gao, L. Mai, C. M. Lieber, *Nat. Nanotechnol.* **2014**, *9*, 142.
- [37] K. Kitamura, B. Judkewitz, M. Kano, W. Denk, M. Häusser, *Nat. Methods* **2008**, *5*, 61.
- [38] M. E. Wagshul, P. K. Eide, J. R. Madsen, *Fluids Barriers CNS* **2011**, *8*, 5.
- [39] E. Musk, *J. Med. Internet Res.* **2019**, *21*, 16194.